CrossMark

A combined parametric shape optimization and ersatz material approach

Fabian Wein[1] · **Michael Stingl**[1]

Abstract This article describes a parametric shape optimization approach using vertical or horizontal structures with a fine parametrization of their center lines and profiles. In this context horizontal means a lateral connection from left to right and vertical means a bottom-up connection. These structures are projected to a pseudo density field associated with a fixed mesh using a differentiable mapping. This enables the use of existing topology optimization tools with respect to the solution of the state problem based on the pseudo density field. The approach belongs to a class of geometry projection onto a fictitious domain methods. It therefore shares the property that sensitivity analysis is reduced to extend the well known gradient calculation from topology optimization by chain using the sensitivity of the mapping from shape variables to pseudo density. The contribution lies in the combination with our specific shape parametrization and the associated regularization. Optimization problems can be formulated concurrently in terms of shape variables and pseudo density. We discuss regularization, periodicity constraints, symmetry formulations and overhang constraints in terms of shape variables. Volume and perimeter constraints are easily formulated in terms of the pseudo density. We see our approach as being particularly beneficial for certain problem classes where it may be difficult to restrict the design space, e.g. restricting isolated structures or holes or where a strict control of solid to void transition is necessary. Consequently, we show examples for phononic band gap maximization, boundary driven heat optimization and perimeter maximization for a flow problem. We also present a formulation of overhang constraints for additive manufacturing in terms of shape variables.

1 Introduction

Topology optimization and shape optimization represent two key approaches to structural optimization. Numerous variants of these approaches with differing degrees of complexity have been proposed. While Sigmund and Maute (2013) have attempted to provide an overview of the range of adaptations proposed, it is almost impossible to provide a comprehensive overview of the field due to the wealth of research opportunities it provides and its consequent dynamic growth.

In the following, we briefly recall the fundamental ideas of density-based topology and shape optimization. To illustrate these ideas, we adopt a stiffness maximization problem for a linear elastic setup discretized by the finite element method as a model.

For density-based topology optimization the standard approach is based on the SIMP[1] model introduced in Bendsøe (1989). Typically the design space consists of all N cells of the simulation mesh. The design variables are called *pseudo density* $\boldsymbol{\rho} \in \mathbb{R}^N$ with each component $\rho_e \in (0, 1]$. In the case considered here, it is necessary to regularize the

✉ Fabian Wein
   fabian.wein@fau.de

   Michael Stingl
   michael.stingl@fau.de

1 Friedrich-Alexander-Universität Erlangen-Nürnberg,
   Zentralinstitut Scientific Computing, Martensstrasse 5a,
   91080 Erlangen, Germany

---

[1] Solid Isotropic Material with Penalization.

design, see Sigmund and Petersson ([1998](#)), e.g. by applying a density filter, see Bruns and Tortorelli ([2001](#)). In the framework of the finite element model, a piecewise constant material approximation is used, which is constructed from local elasticity tensors $[c]_e(\rho) = \mu_e(\rho)\,[c]_0$ parametrized by the function $\mu_e(\rho) \in (0, 1]$ and a given material $[c]_0$. The function $\mu : \mathbb{R}^N \to \mathbb{R}^N$ may contain the density filter and a nonlinear mapping, like the power law, to drive the components of the *physical pseudo density* $\widetilde{\rho} = \mu(\rho)$ toward the bounds zero and one, as only these have a straightforward physical interpretation as void and solid, respectively.

Despite being extremely versatile, powerful and successful in both academic and industrial real world applications, density-based topology optimization in its basic form is remarkably easy to implement and apply. Regarding implementation we refer to the famous 99-lines implementation in MATLAB, Sigmund ([2001](#)), and the subsequent implementation by Andreassen et al. ([2011](#)). In a particular sense, topology optimization is easy to use as no preliminary design is required - one starts with a constant density on a regular mesh of uniform quadrilaterals or hexahedrons.

However, density-based topology optimization has one drawback: the representation of the boundary between solid and void. Due to regularization this interface is generally blurred by some layers of cells with intermediate values of physical pseudo density. This effect can be reduced by projection methods (based on Guest et al. ([2004](#)), see also Sigmund ([2007](#))). If, however, in the extreme case a perfect solid-void physical design is achieved, any curved boundary is subject to jagged edges. The standard remedy is finer mesh resolution, but due to the uniform regular mesh a global refinement is required that is computationally rather expensive.[2]

A large class of design constraints, such as minimal/maximal feature size constraints, are modeled indirectly by the aforementioned projection-based filters, see Guest et al. ([2004](#)) and Guest ([2009](#)), respectively. Also robust design (Wang et al. [2011](#)) or even overhang conditions for additive manufacturing (Langelaar [2017](#)) and many more design requirements are realized by filters. A recent overview with detailed discussion can be found in Lazarov et al. ([2016](#)). This implicit handling of design constraints is very efficient given the large number of design variables in density-based topology optimization, ranging from numbers in the thousands to numbers in the millions. However, expressing design constraints implicitly has its limits as we will see later in the course of this paper.

In contrast to density-based topology optimization, in shape optimization structures are defined by their surfaces. The mathematical approach is typically formulated in an infinite dimensional setting, see e.g. Sokolowski and Zolesio ([1992](#)) or Haslinger and Mäkinen ([2003](#)). An initial design must be provided for shape optimization. In general, the optimization method conserves topology, i.e. the number of holes remains constant. Hence, the topology of the initial design restricts the admissible shapes and thus has great influence on the quality of the optimal design. There are methods available to overcome this restriction, e. g. by insertion of holes based on the topological derivative, see Novotny and Sokołowski ([2012](#)). However, this is an involved process in terms of theory and technical implementation.

For numerical realization of the shape optimization, the initial design has to be tessellated to solve the state problem. In contrast to topology optimization only the structure and not the void is treated, which can save a significant part of the computational cost but loses the simplicity of a uniform mesh. As the shape is defined by the surface of the mesh, the boundary nodes must be moved within optimization according to the shape derivative. This leads to issues with mesh quality, necessitating common techniques such as mesh smoothing and/or remeshing. These issues were recently addressed in Christiansen et al. ([2015](#)), however, with an implicit shape handling. Alternatively, the shape derivative may be expanded from the boundary to the interior nodes by solving an additional partial differential equation, which leads to a more robust mesh deformation, see e.g. Gangl et al. ([2015](#)) or Semmler et al. ([2015](#)).

Using each surface node in shape optimization as a design variable is called the independent node movement approach as described by Imam ([1982](#)). An alternative approach is the parameter-free shape optimization. This approach differs from parametric shape optimization in that it requires no parametrization from the user. While it provides a large space of admissible shapes, it also comes with its own challenges in terms of regularization and feature size control, see e.g. Le et al. ([2011](#)). In the course of the optimization process, insertion or deletion of boundary nodes may be necessary. This generally prevents the use of first order black-box optimizers, like implementations of MMA (Svanberg [1987](#)) or SNOPT (Gill et al. [2002](#)). As a consequence, constraint functions need to be handled indirectly. Furthermore, no rigorous convergence criteria are available.

In classical shape optimization the surface is indirectly parametrized by a small number of parameters, see e.g. Haftka and Grandhi ([1986](#)). Conveniently, this corresponds to the construction of geometries by spline functions in computer aided design (CAD). Here, the mapping from the design parameters onto the boundary nodes is differentiable and thus allows gradient based optimization, see Braibant and Fleury ([1984](#)). In contrast to parameter-free shape optimization, the number of design variables is finite and fixed, allowing the use of state-of-the-art black-box optimizers.

---

[2]Local mesh refinement, as in Maute and Ramm ([1995](#)), does not appear to be widely applied.

The choice of the parametrization is a critical task for the user in determining the optimized design. The design freedom in shape optimization is typically small in comparison to topology optimization, thus the user requires a much clearer idea of the intended design. However, for some applications, this is more a feature than a limitation, consider e.g. wing profile design or sizing of a lattice.

There is a further important class of structural optimization we want to mention only briefly. Level-set methods in their most common approaches perform shape optimization on a fixed grid such that remeshing is not an issue. Interfaces can be crisp and certain topological changes come without difficulties. We refer to the excellent review paper (van Dijk et al. 2013). Indeed, the geometry projection methods introduced below have some similarities with some approaches of the level-set method, e.g. the property of being topology optimization methods and the way geometries are projected onto the analysis mesh.

In this paper, we integrate parametric shape optimization into a topology optimization setup, generating the discrete vector of pseudo densities $\boldsymbol{\rho}$ from shape parameters $\boldsymbol{s}$ by a differentiable mapping $T : \boldsymbol{s} \mapsto \boldsymbol{\rho}$. Our method thereby belongs to a class of geometry to fictitious domain projection methods, with which we share the basic properties. For the pseudo density based parametrization of the finite element model (including possible adjoint systems) and the calculation of the gradient, any existing topology optimization implementation can be used without modification. There is even no requirement for filtering and penalization, resulting in a *one-field SIMP* model following the notation of Sigmund and Maute (2013), as there is no distinction between pseudo and physical density fields. In general, the parametrization of the geometry can be arbitrary. However, in this article we investigate a very simple shape parametrization based on structures using sizing and geometry parameters. Our parameters explicitly describe location and width of geometries. Geometries are also used for thickness control in density-based topology optimization by Zhou et al. (2015) and the level set method by Allaire et al. (2016), however, the geometries and their location are given implicitly.

The mentioned class of geometry projection methods encompasses methods where low dimensional geometries are projected onto a fixed discretization. Some approaches appear to have been developed independently, but early references can be found with respect to shape optimization based on a fixed mesh. The analysis of the infinite dimensional setting of so called fictitious domain methods in shape optimization without an intermediate mapping function is given in Haslinger and Mäkinen (2003), i.e. a mesh cell is either solid or void. In Norato et al. (2004) a filter type mechanism is added, leading to a smooth mapping resulting in intermediate density values at the boundary. In

Norato et al. (2004) a single explicit geometry (an ellipse) is used and analyzed thoroughly. Also an implicit boundary is formed based on a polygonization of a fixed set of radial basis functions, albeit no further details are given. The implicit design description by a union of geometrical primitives has been presented by Saxena and coworkers in the form of the *Material Mask Overlay Strategy* (MMOS). In Saxena (2008) and several following publications with similar content, circular objects of solid or void are introduced with the design variables location, radius and a solid/void flag. These objects may overlap and the optimization is performed via a gradient-free genetic algorithm. In Saxena (2011) only circular void objects are considered and the mapping onto pseudo density values is performed via a smoothed Heaviside function such that gradient-based optimization can be applied. The void objects can arbitrarily overlap and the shape of the solid design is only implicitly given as the complement of the union the void objects. Other work using freely movable solid or void objects modeled by varying geometric primitives includes (Zhang et al. 2016) using quadrilaterals, who call their method *moving morphable components* (MMCs). Bars with half circular ends are used in Norato et al. (2015), who call their method *geometry projection*. The same objects are used in Hoang and Jang (2016), with a different geometry-to-density mapping and handling of overlaps. All the methods which are based on the aggregation of many primitive geometries share the fact that holes can appear arbitrarily, we therefore consider them as topology optimization methods. Shape optimization projected onto a fictitious domain can be found with an implicit shape representation in Norato et al. (2015), based on radial basis functions, and Dunning (2017) based on a level set approach. In Gersborg and Andreasen (2011) Heaviside projection topology optimization is shown for single horizontal variables. This could be seen a simplified single vertical structure of our approach. However, it is more similar to a reduced topology optimization.

We have specific optimization problems in mind where the design freedom of topology optimization is in some way too large and the exclusion of undesired designs is difficult. For a number of examples, see Section 4. For such problems the restricted and tightly controllable design freedom of parametric shape optimization is beneficial. The proposed shape mapping approach is accompanied by the easy mesh handling of topology optimization rather than the issues mentioned above in classical shape optimization. As a trade-off we have to accept the blurred and rasterized boundary known from topology optimization, albeit we have more control on the transition zone than in topology optimization. An additional motivation for the approach might be the use of numerical methods, such as Lattice Boltzmann Methods or the Discrete Dipole Approximation (Yurkin and Hoekstra 2007), which greatly rely on a uniform mesh and are

thus difficult to combine with classical shape optimization methods.

The method we present here is focused on only a few richly parametrized structures in contrast to many simple parametrized geometric objects. We view the resultant reduced and tightly tunable design space as a beneficial feature for certain problem classes. A special feature of our parametrization is, that we have the first and second order derivatives of the shape design variables in the sense of local constraints at hand, with allows a precise regularization of the problem. In this sense, our method is close to classical parametrized shape optimization. However, mesh handling does not need to be implemented and existing topology optimization code can be reused. Moreover, design based criteria like resource and perimeter constraints are very easy to formulate based on density values.

The paper is organized as follows. Section 2 introduces the shape parametrization as well as the density mapping and discusses associated smoothness issues. In Section 3 we address shape regularization and symmetry handling. Section 4 provides examples where we benefit from shape mapping compared to topology optimization and conclusions are provided in Section 5.

2 Design parametrization

Throughout this paper we consider a design composed from a set S of horizontal and vertical strips. In the following discussion we begin with a single horizontal strip S as depicted in Fig. 1. Vertical strips are treated accordingly, multiple and overlapping structures are discussed in Section 2.2. For illustrative purposes, we use standard compliance minimization examples in this section, being aware that parametrized shape optimization is not necessarily beneficial for this application.

2.1 Single structure

We assume the unit square $\Omega = [0, 1]^2$ as the design domain, regularly discretized by N^2 quadrilateral finite elements Ω_e as in Fig. 1. We now introduce fixed horizontal coordinates

$$\overline{x}_i = \frac{i - 1}{N}, \ i = 1, \dots, N + 1.$$

Assigned with these coordinates, we define the map

$$I : [0, 1] \rightarrow \{1, \dots, N + 1\}$$
$$x_1 \mapsto \lfloor x_1 N \rfloor + 1,$$

where $\lfloor \cdot \rfloor$ is the floor function.

The horizontal strip is described by center nodes

$$\boldsymbol{a}_i(a_i) = (\overline{x}_i, a_i)^\top, \ 1 \leq i \leq N + 1, \tag{1}$$
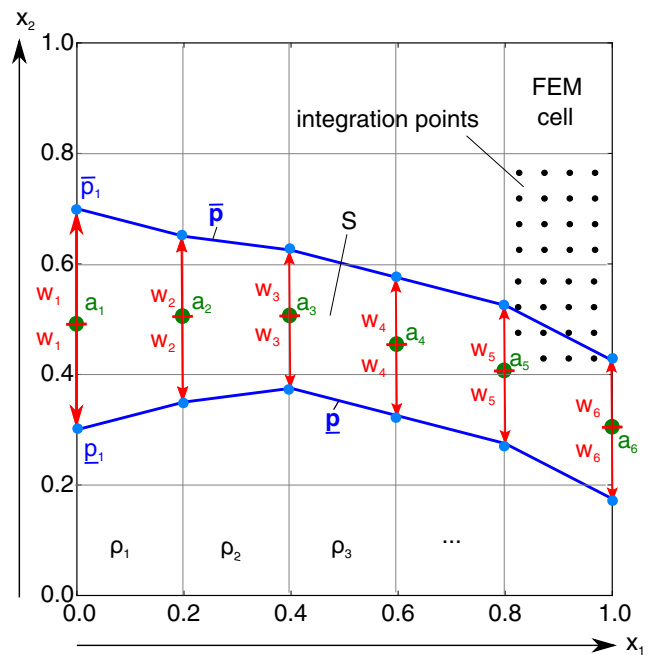

Fig. 1 Based on a square 5×5 grid, a single parametrized horizontal structure is defined. The $N + 1$ variables $a_1, \dots, a_6$ (green) denote the height in x_2 coordinates of the center line of the strip at the x_1 positions $0.0, 0.1, \dots, 1.0$. The corresponding points $\boldsymbol{a}_1, \dots, \boldsymbol{a}_6$ are given by (1). The profile variables $w_1, \dots, w_6$ (red) give the half strip height in $\pm x_2$ direction, see (2) and (3). The discrete vector of nodal design variables $(a_1, \dots, a_6)$ is denoted as $\boldsymbol{a}$, the discrete vector of profile variables $(w_1, \dots, w_6)$ is denoted as $\boldsymbol{w}$

where $A_-^* \leq a_i \leq A_+^*$ are *nodal* design variables. With *profile* design variables w_i, we further define for all $1 \leq i \leq N + 1$ points

$$\overline{\boldsymbol{p}}_i(a_i, w_i) = (\overline{x}_i, a_i + w_i)^\top \tag{2}$$
$$\underline{\boldsymbol{p}}_i(a_i, w_i) = (\overline{x}_i, a_i - w_i)^\top. \tag{3}$$

The design variables form the vector of nodal variables $\boldsymbol{a} = (a_1, a_2, \dots, a_{N+1})$ and profile variables $\boldsymbol{w} = (w_1, w_2, \dots, w_{N+1})$. Using (2) and (3) we introduce the piecewise linear functions

$$\overline{\boldsymbol{p}}(\boldsymbol{a}, \boldsymbol{w}; x_1) = t(x_1) \, \overline{\boldsymbol{p}}_{I(x_1)} + (1 - t(x_1)) \, \overline{\boldsymbol{p}}_{I(x_1)+1} \tag{4}$$
$$\underline{\boldsymbol{p}}(\boldsymbol{a}, \boldsymbol{w}; x_1) = t(x_1) \, \underline{\boldsymbol{p}}_{I(x_1)} + (1 - t(x_1)) \, \underline{\boldsymbol{p}}_{I(x_1)+1}, \tag{5}$$

with $t(x_1) = N (x_1 - \overline{x}_{I(x_1)})$ for $0 \leq x_1 \leq 1$, which defines the lower and upper boundary of the single horizontal structure $S(\boldsymbol{a}, \boldsymbol{w})$.

2.1.1 The shape mapping T

With $a(x_1)$ and $w(x_1)$ we denote the linear interpolation of the corresponding variables $a_{I(x_1)}$ and $a_{I(x_1)+1}$, $w_{I(x_1)}$ and $w_{I(x_1)+1}$, respectively, constructed precisely as in (4). For brevity of notation we do not explicitly note the dependence

of a and w on the design variables $\boldsymbol{a}$ and $\boldsymbol{w}$. The structure $S(\boldsymbol{a}, \boldsymbol{w})$ can be expressed by a height function with values 1 within the structure and 0 outside. A smoothed one-dimensional height function is shown in Fig. 2 and given as

$$
t_\beta(a(x_1), w(x_1), x_2) = \begin{cases} 1 - \dfrac{1}{e^{\beta(x_2 - a(x_1) + w(x_1))} + 1} \\ \dfrac{1}{e^{\beta(x_2 - a(x_1) - w(x_1))} + 1} \end{cases},
$$

where the first case $1 - \ldots$ holds for $x_2 \leq a(x_1)$, corresponding to the left section in Fig. 2 and $\beta > 0$ is a smoothing parameter. The function is based on scaled and shifted hyperbolic tangent functions. Note that the function approaches 0 and 1 arbitrary fast with sufficient high β, but analytically never reaches 0 and 1. However, the non-differentiability of t_β for $x_2 = a(x_1)$ is purely theoretical and numerically unimportant, see also Section 2.1.5.

Now the pseudo density variables ρ_e with $1 \leq e \leq N^2$ are assigned to finite elements and evaluated as $\rho_e = T_e(\boldsymbol{a}, \boldsymbol{w})$ with

$$
T_e : \mathbb{R}^{N+1} \times \mathbb{R}^{N+1} \to [\rho_{\min}, 1]
$$

and

$$
T_e(\boldsymbol{a}, \boldsymbol{w}) = \rho_{\min} + (1 - \rho_{\min}) \int_{\Omega_e} t_\beta(a(x_1), w(x_1); x_2) \, \mathrm{d}(x_1, x_2).
$$
(6)

The integration is performed numerically using sufficiently many integration points.

The partial derivatives $\frac{\partial t_\beta}{\partial a_i}$ and $\frac{\partial t_\beta}{\partial w_i}$ are easy to calculate and depicted in Fig. 3. See also Section 2.1.5 for a discussion of the differentiability of T_e with respect to the profile width and β.
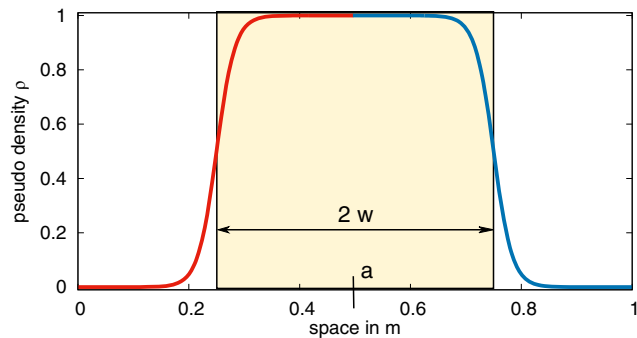

Fig. 2 The smoothed height function $t_\beta(a(x_1), w(x_1); x_2)$ to be evaluated at each integration point, see Fig. 1
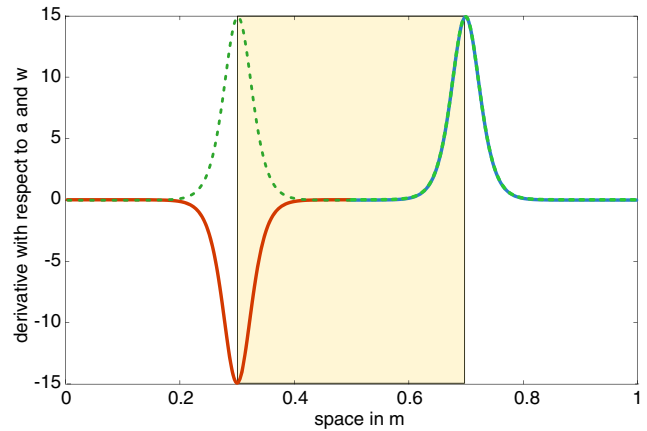

Fig. 3 The derivatives of $t_\beta(a(x_1), w(x_1); x_2)$ (Fig. 2) with respect to the nodal position a (solid) and profile thickness w (dashed)

2.1.2 Model problem

We now formulate a first parametric shape optimization problem in algebraic form:

$$
\min_{\boldsymbol{a}, \boldsymbol{w}} \quad \boldsymbol{f}^\top \boldsymbol{u}
$$
(7)

$$
\text{s.t.:} \ \boldsymbol{K}(\boldsymbol{\rho}) \, \boldsymbol{u} = \boldsymbol{f}
$$
(8)

$$
\rho_e = T_e(\boldsymbol{a}, \boldsymbol{w}), \quad 1 \leq e \leq N^2
$$
(9)

$$
v(\boldsymbol{\rho}) = \frac{1}{N^2} \sum_{e=1}^{N^2} \rho_e \leq V^*
$$
(10)

$$
\boldsymbol{a} \in [0, 1]^{N+1}
$$
(11)

$$
\boldsymbol{w} \in [W_-^*, W_+^*]^{N+1}.
$$
(12)

The compliance minimization problem (7) is formulated in terms of the shape variables $\boldsymbol{a}$ and $\boldsymbol{w}$. The state problem (8) is formulated in terms of pseudo density $\boldsymbol{\rho}$. Both the state problem and the mapping T from the shape variables to $\boldsymbol{\rho}$ (9) are treated implicitly. Note that the resource constraint (10) is formulated in $\boldsymbol{\rho}$. There is no direct resource constraint on the shape variables. The bounds of the shape variables are given in terms of the unit meter. We assume as design domain a unit square, hence every nodal variable a_i may take any value within the full x_2 range.

2.1.3 Sensitivity analysis

In topology optimization, it is well known how the sensitivities $\frac{\partial \boldsymbol{f}^\top \boldsymbol{u}(\boldsymbol{\rho})}{\partial \boldsymbol{\rho}}$ and $\frac{\partial v(\boldsymbol{\rho})}{\partial \boldsymbol{\rho}}$ are obtained. The derivative of any function $f(\boldsymbol{\rho}(\boldsymbol{a}, \boldsymbol{w}))$ with respect to s, either the nodal position a or profile w, is given by the chain rule as

$$
\frac{\partial f}{\partial s_i} = \sum_{e=1}^{N^2} \frac{\partial f}{\partial \rho_e} \frac{\partial T_e}{\partial s_i}.
$$
(13)

We note that at most $2N$ summands of N^2 are non-zero.

(a) pseudo density   (b) optimized shape variables   (c) SIMP reference
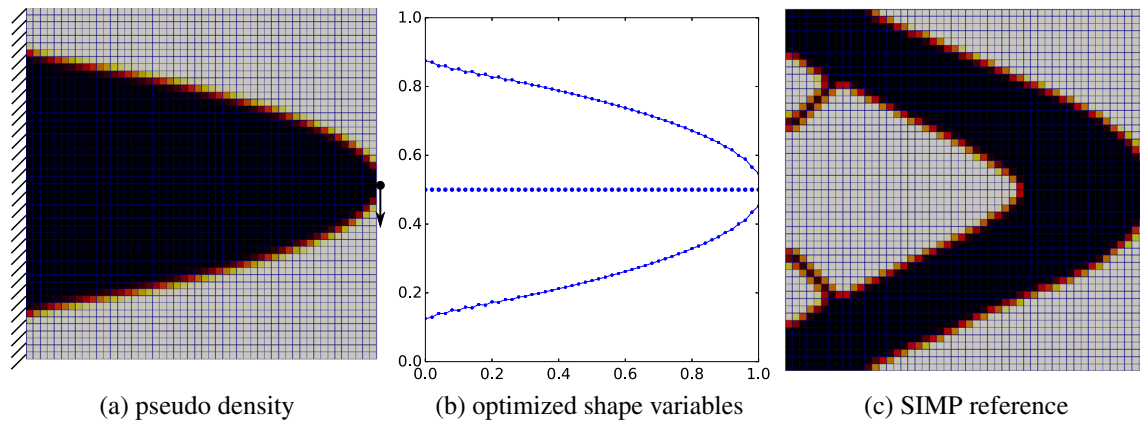
Fig. 4 The test case for the single horizontal structure example of Section 2.1.2: **a** optimized shape mapped to pseudo density; **b** visualization of optimal shape variables. The nodal positions a_i stay at their initial position 0.5; **c** standard SIMP optimization result as reference. The compliance in (**a**) is 67% worse than the SIMP result

2.1.4 A Single structure example

Figure 4a shows the setup for the symmetric single structure compliance minimization problem (7)...(9). The volume is restricted to 50%. Initial value for all design parameters are $a_i = .5$ and $w_i = .25$. The discretization is $N = 50$ which holds for all examples, if not noted otherwise. The profile is practically unbounded with $W_-^* = 0.005$ and $W_+^* = 0.5$, β is chosen as 75. Figure 4b displays the optimized shape variables.

The shape gradient (13) collects the sensitivities with respect to ρ only at the boundary of the shape. This is due to the construction of t_β, see Fig. 3; within or outside of the structure $\frac{\partial t_\beta}{\partial a_i}$ and $\frac{\partial t_\beta}{\partial w_i}$ quickly approach zero. Evaluating the sensitivities at the integration points of (6), we can visualize the gradient mapped to the design domain. Figure 3 shows that location but not the value varies, therefore we visualize in Fig. 5b the profile sensitivity weighted by the compliance gradient of Fig. 5a. As expected, the gradient is constant in the optimum, see also the bottom line in Fig. 5c.

The curve for the final profile sensitivity in Fig. 5c shows for the first and last shape variable only half the magnitude. This is explained by (13) where only N instead of $2N$ non-zero summands correspond with the first and last shape variables. The sensitivity of the nodal variables has a positive and negative value on the shape boundary. With the symmetric $\frac{\partial f^\top u}{\partial \rho_e}$ the shape derivatives sums to zero in the initial and final design, as shown in the upper line in Fig. 5c.

2.1.5 Minimal profile width

Considering t_β in Fig. 2 with $w = 0$, a kink with height 0.5 would appear. By integration in (6), the resulting unscaled pseudo density would always be smaller 0.5. The kink is clearly non-differentiable and therefore to be avoided. To this end we are interested in a minimal profile variable w, which guarantees a sufficiently smooth structure representation. The function t_β becomes smooth when the tangent for the left and right side of t_β in a is sufficiently flat. This means that the derivative of t_β, see Fig. 3, approaches zero

(a) final $\frac{\partial f^\top u}{\partial \rho_e}$ (b) final $\frac{\partial f^\top u}{\partial \rho_e} \sum_i \frac{\partial \rho_e}{\partial s_i}$ (c) $\frac{\partial f^\top u}{\partial a_i}$ and $\frac{\partial f^\top u}{\partial w_i}$
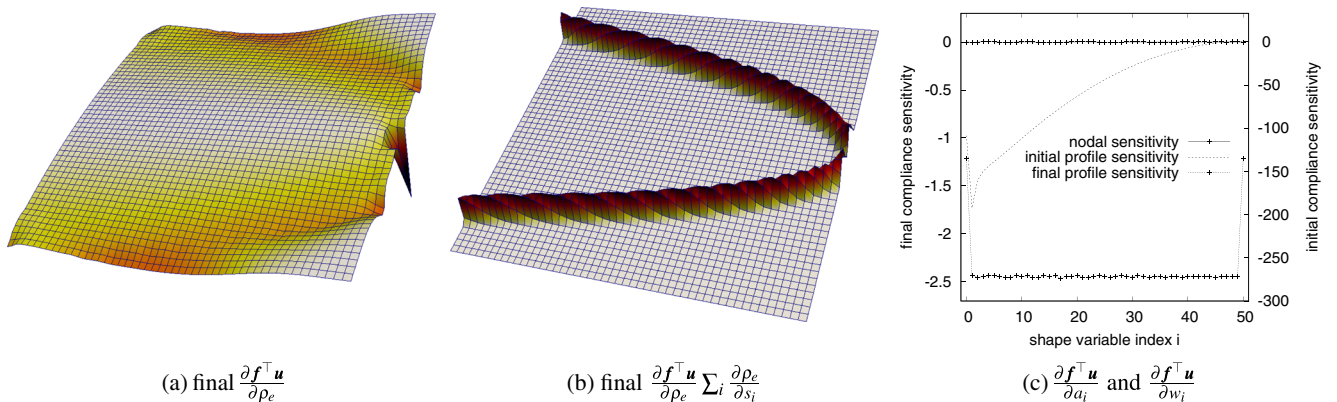
Fig. 5 Visualization of the sensitivities for the single structure example in Fig. 4: **a** sensitivity of the compliance w.r.t. ρ as in topology optimization; **b** taking the influence of the profile variables into account, see Fig. 3; **c** sensitivities of the shape variables, see (13)

close enough. Note that zero can be approached only asymptotically. Thus our goal is to derive a bound for w such that the none-smoothness in a is sufficiently small.

The left side of $\partial t_\beta / \partial w$ is given as

$$\frac{\partial t_\beta(a, w, x, \beta)}{\partial w} = \frac{\beta \, e^{\beta \, (x-a+w)}}{(e^{\beta \, (x-a+w)} + 1)^2}.$$

To have a sufficiently smooth transition we require

$$\frac{\partial t_\beta(a = x, w, \beta)}{\partial w} \leq \epsilon.$$

Solving for w, we obtain

$$w(\beta, \epsilon) = \frac{\ln\left(\frac{\beta - 2\epsilon + \sqrt{\beta^2 - 4\beta\epsilon}}{2\epsilon}\right)}{\beta} \approx \frac{\ln\frac{\beta}{\epsilon}}{\beta}, \quad (14)$$

depicted in Fig. 6. For a small profile variable w large β is required. This also means that for small β the bound W_-^* needs to be sufficiently large according to (14).

In the sense of β-continuation, W_-^* might be subject to adjustment also. In the presence of a volume constraint this might have a significant impact on the design. Fortunately β-continuation is not necessary to the author's experience.

Leaving the non-differentiability issue aside, the profile variable w could get negative such that structure vanishes completely.

2.2 Overlapping structures

The single structure cantilever in Fig. 4a performs relatively poorly, with a compliance 76% higher than the standard SIMP solution shown in Fig. 4c. Obviously a single structure design space is too restrictive for the problem, which requires multiple structures.
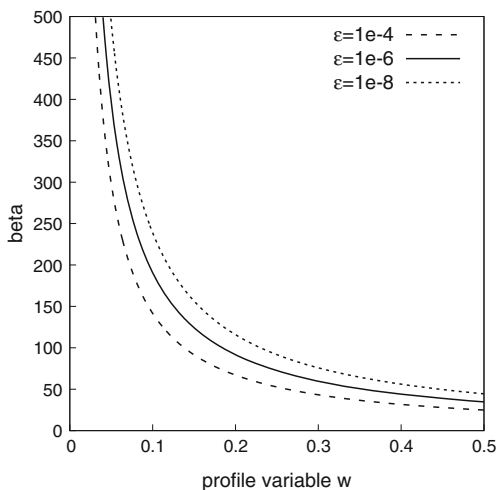
In the following, the set of horizontal or vertical structures S is denoted as $\boldsymbol{S}$. The linear interpolations of the nodal and profile variables now depend on the structure S and the parameter x_1.

We discuss two approaches to handle overlapping of multiple structures. To this end, we extend (6) as

$$T_e(\boldsymbol{a}, \boldsymbol{w}, \boldsymbol{S}) = \rho_{\min} + (1 - \rho_{\min}) \, T_e^{(\cdot)}(\boldsymbol{a}, \boldsymbol{w}, \boldsymbol{S}),$$

where $T_e^{(\cdot)}$ is either given by (15) or (16). The first approach

$$T_e^{\max} = \int_{\Omega_e} \max_S \left(t_\beta(a(S, x_1), w(S, x_1); x_2) \right) \, \mathrm{d}(x_1, x_2) \quad (15)$$

simply chooses for every integration point the structure with the highest value which contributes to ρ_e and to the derivative $\frac{\partial T_e}{\partial s}$. The resulting density distribution is depicted in Fig. 7a. In Fig. 7c the sensitivity with respect to the nodal shape parameters is shown. Due to the max operator in (15) this approach is not differentiable.

A smooth approach is given by

$$T_e^\tau = \int_{\Omega_e} \tau \left(\sum_S t_{\beta/2}(x_2, a(S, x_1), w(S, x_1)) \right) \, \mathrm{d}(x_1, x_2), \quad (16)$$

where the density values of all shapes are summed to $\tilde{\rho}$ and limited to $\rho_{\max} = 1$ by the smooth function τ

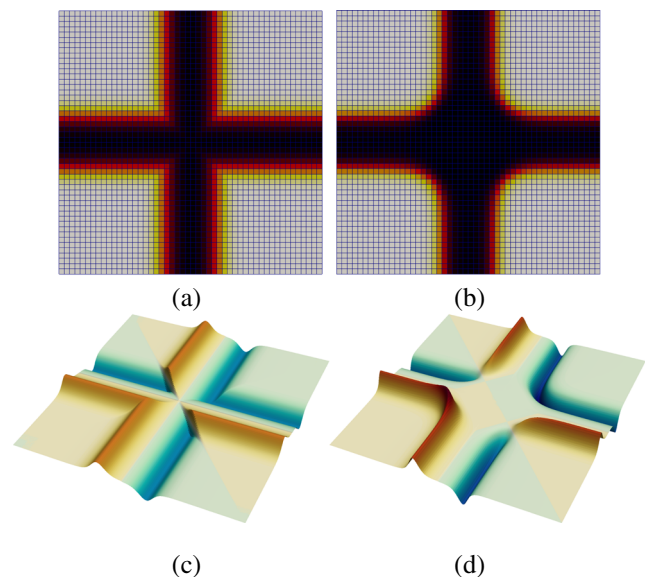$$\tau(\tilde{\rho}) = 1 - \frac{1}{e^{11 \, (\tilde{\rho} - .5)} + 1}. \quad (17)$$

Fig. 7 Two approaches to overlap structures: **a** The non-smooth max approach (15) and its sensitivity with respect to the nodal shape parameters (**c**); **b** and **d** show the differentiable approach (16) based on the smoothing function τ (17), see also Fig. 8. Note that ρ is piecewise constant on the finite elements but the sensitivities are evaluated on the level of integration points

Fig. 6 Relationship of minimal profile variable w and β according to (14). If the desired minimal profile width variable is 0.1, one has to choose $\beta \geq 200$ with a smoothness criterion $\epsilon = 1 \cdot 10^{-8}$, see (14)

The resulting density distribution is shown in Fig. 7b and the sensitivity with respect to the nodal shape parameters is shown in (d). To compensate the effect of τ, we parametrize t with $\beta/2$. In Fig. 8 two shapes $t_\beta(a)$ and $t_\beta(b)$ are shown. These functions are sufficiently well reproduced by $\tau(t_{\beta/2}(a))$ and $\tau(t_{\beta/2}(b))$. The effect of treating two overlapping structures by (16) is illustrated in Fig. 8.

3 Optimization models based on the shape mapping

3.1 Regularization

We extend and solve the model problem (7) ... (9) with two horizontal shapes, hence doubling the number of variables. The parameters are the same as in Section 2.1.4. The resulting density shown in Fig. 9, is not only similar to the topology optimized design in Fig. 4c but even has a slightly better compliance. This is possible because the density filter for the SIMP design does not directly correspond to the β value for the shape mapping problem (here $\beta = 75$). The visualization of the shape variables in Fig. 9 reveals a jagged shape boundary which can also be observed to a less extend in Fig. 4b. This reminds of issues found in classical shape optimization when each boundary node is a design variable. In shape optimization the reason is given as abuse of numerical finite element approximations akin the checkerboards in density-based topology optimization, see references given in Le et al. (2011). Seemingly this effect also holds for the projected density-based design, albeit not visually perceivable with the pseudo density field generated by (16).

In contrast to choosing a coarser and/or higher order boundary representation or variable filtering as in Le et al.
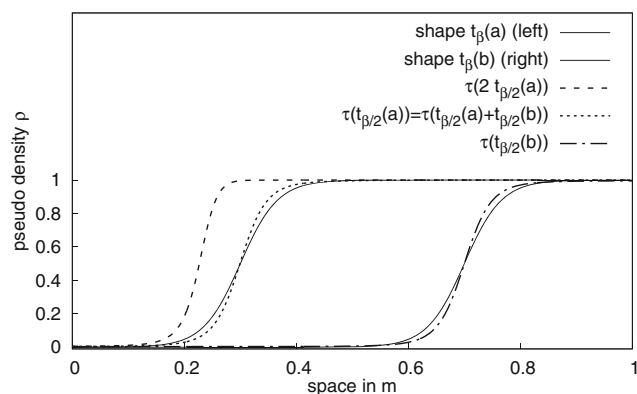

Fig. 8 Visualization of the shape overlapping T_e^τ (16) applied in Fig. 7b: applying $\tau(\tilde{\rho})$ to the sum of two shifted shapes the contribution of the right shape is perfectly canceled. Moving the right structure to the left, essentially doubling a single shape, the resulting function differs significantly from the original shape

(2011) we choose to control the first and second spatial derivative of the shape variables. The single structure problem (7) ... (9) extended to a regularized two structure problem is given as

$$\min_{a, w} \quad f^\top u \tag{18}$$

$$\text{s.t.:} \; K(\rho) \, u = f \tag{19}$$

$$\rho_e = T_e^\tau(a, w), \quad 1 \le e \le N^2 \tag{20}$$

$$v(\rho) \le V^* \tag{21}$$

$$|a_i - a_{i+1}| \le a^*/N, \quad i \in I_1 \cup I_2 \tag{22}$$

$$|w_i - w_{i+1}| \le w^*/N, \quad i \in I_1 \cup I_2 \tag{23}$$

$$|a_{i-1} - 2\,a_i + a_{i+1}| \le c^*/N, \quad i \in Y_1 \cup Y_2 \tag{24}$$

$$a_i \in [0, 1]^{2(N+1)} \tag{25}$$

$$w_i \in [W_-^*, W_+^*]^{2(N+1)}, \tag{26}$$

with the index sets $I_1 = \{[1, \ldots, N], I_2 = \{N + 2, \ldots, 2N + 1\}, Y_1 = \{2, \ldots, N\}$ and $Y_2 = \{N + 3, \ldots, 2N + 1\}$.

The positional and profile shape variables are regularized by slope constraints. The discrete control of the spacial gradient of design parameters was first introduced to topology optimization in Petersson and Sigmund (1998). However, it did not find much application in topology optimization due to the large number of local constraints with $O(2\,N^2)$ for two space dimensions. In (22), the constant a^* allows global control on the design space. With a horizontal spacing of $1/N$ and a maximal vertical spacing $|a_{i+1} - a_i| = 1/N$, the slope is $|1|$ which corresponds to $45°$. We usually choose a^* slightly larger than 1 such that a global rotation of the structure by $\approx 45°$ is feasible. As the direction of the profile width variable is axis aligned and not orthogonal to the orientation of the structure, the actual minimal width of the structure depends on that angle and is by a factor of $\sqrt{\frac{1}{2}}$ for $45°$ thinner than for the axis aligned case. The same way, prescribed and maximal thickness can be achieved, but clearly not precisely as the cross-section diameter. The slope regularization of the profile variables (23) has a much lower impact, we usually choose w^* to $a^*/2$.

Note that within the bounded slope undesired high oscillations of the boundary are still feasible. However, choosing the slope bounds tighter might have a significant impact on the achievable design. A more local control is accomplished by the curvature constraint (24). The parameter c^* gives direct control on the smoothness of the shapes and is an

Fig. 9 A variant of the problem depicted in Fig. 4 with two horizontal structures without regularization
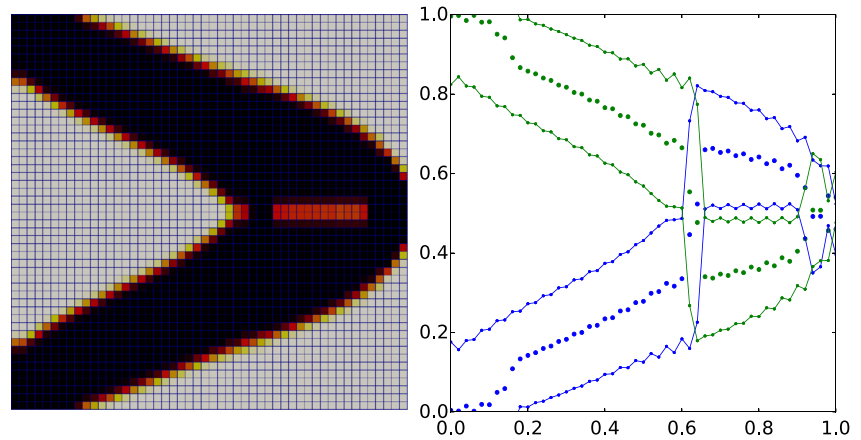
important tuning parameter. An appropriate choice depends on the particular problem setting, here we let $c^* = 0.2$. For the profile variables, usually no curvature constraints are necessary.

Note that slope and curvature constraints cannot supersede each other. While slope constraints have a more global control of the design, curvature constraints control the local smoothness.

Figure 10 shows the design obtained for problem (18) ... (26). The shape variables are regularized and result in an almost identical mapped pseudo density distribution. The optimization process benefits from the regularization as it requires only a third of the iterations. The principal design was obtained after eight iterations.

3.2 Control of the design

3.2.1 Periodic structures

A simple way to enforce periodic structures is via the constraints

$$
\begin{aligned}
|a_k - a_{k+N+1}| &= 0, \\
|w_k - w_{k+N+1}| &= 0,
\end{aligned}
\tag{27}
$$

where $k \in \{1, N + 2, 2(N + 1) + 1, \ldots\}$. Alternatively one of the variables could be eliminated, but with the given formulation, the constraints can be easily relaxed by inequality constraints or used to formulate anti-periodic constraints. When we use the periodicity constraint we also adapt the constraints for slope and curvature control.[3] There an additional slope constraint

$$
\begin{aligned}
|a_1 - a_{N+1}| &\le a^*/N \\
|w_1 - w_{N+1}| &\le w^*/N
\end{aligned}
$$

---

[3]We note that the periodic design constraint is no replacement for periodic boundary conditions on the state problem.

and additional curvature constraints

$$
\begin{aligned}
|a_{N+1} - 2\,a_1 + a_2| &\le c^*/N \\
|a_N - 2\,a_{N+1} + a_1| &\le c^*/N.
\end{aligned}
$$

Figure 11 shows as a reference the solution of a particular test case without periodicity constraints. The parameters follow Section 2.1.4, however the discretization is increased to $N = 100$. The design composed by one horizontal and one vertical structure is very close to a corresponding SIMP result. In Fig. 12 the periodicity constraints (27) are applied. Also slope (22) and curvature (24) constraints are modified with respect to periodicity. The compliance of the periodic design is 7.3% worse than in the reference case.

3.2.2 Symmetric structures

Symmetric designs are easily realized by repeating design variables. For instance, the square symmetric structure to be used in Section 4.1 can be generated by three reflections as shown in Fig. 13. Restricting the discussion to nodal shape parameters, there are $4\,(N + 1)$ parameters of which only $N/2$ are actually free design parameters. We assume the parameters of the horizontal structure in the lower left quadrant as design variables (left part of the blue structure in Fig. 13). The remaining part of this structure in the lower right quadrant is given by the equation

$$
\boldsymbol{a}_{N-i} = (x(i), a_i)^\top, \ i \in [1, N/2].
$$

The resulting horizontal structure is reflected horizontally to a second structure (here the green structure in the upper quadrants) via

$$
\boldsymbol{a}_{(N+1)+i} = (x(i), 1 - a_i)^\top, \ i \in [1, N + 1].
$$

Finally, the first structure is reflected diagonally twice to the red and cyan structures, realized by the equations

$$
\begin{aligned}
\boldsymbol{a}_{2(N+1)+i} &= (a_i, x(i))^\top, \ i \in [1, N + 1], \\
\boldsymbol{a}_{3(N+1)+i} &= (1 - a_i, x(i))^\top, \ i \in [1, N + 1].
\end{aligned}
$$

Fig. 10 Regularized variant of the problem depicted in Fig. 9 with almost identical resulting compliance. The only visual difference in the pseudo density field is a solid 2 × 2 block in the left part of the gap
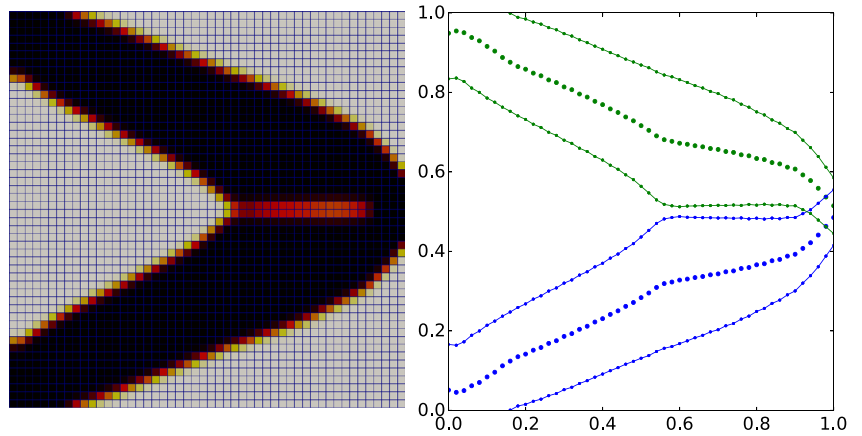

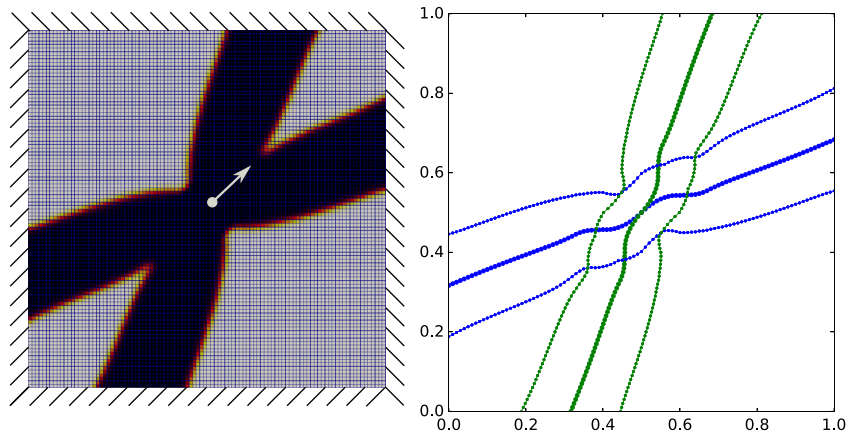**Fig. 11** A diagonal central force is applied within a fully supported domain

Fig. 12 The problem in Fig. 11 with periodicity constraints (27) and periodic slope and curvature constraints
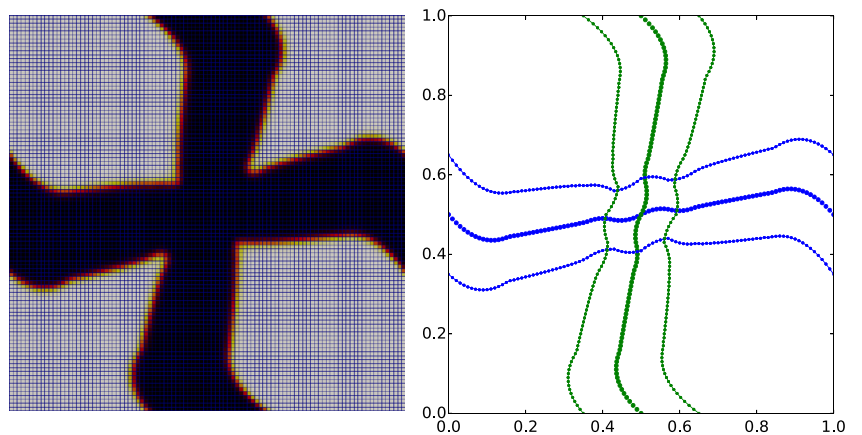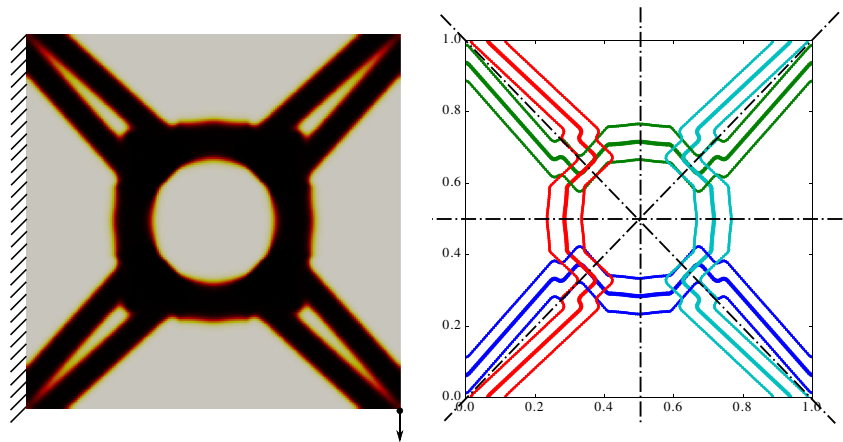
Fig. 13 Compliance minimization for a square symmetric design with four symmetry axes. The design consists of two horizontal and two vertical structures with only 1/8 of the parameters being free design parameters. The profile is fixed to 0.05, $\beta = 75$, $N = 200$

3.2.3 Overhang constraints

In additive manufacturing, overhanging structures are typically difficult to realize. Two standard remedies are to add support structures to be removed after manufacturing and/ or a limit on the angle of overhanging structures. In the context of topology optimization (Gaynor and Guest 2016) and (Langelaar 2017) presented density filter based approaches. We also refer to this work for more background information about the topic.

The principal idea in realizing overhang constraints with shape mapping is to apply slope constraints on the interface nodes $a_i \pm w_i$. Horizontal and vertical structures need different constraints, see Fig. 14. For a horizontal structure only the lower boundary nodes $a_i - w_i$ need to fulfill local constraints

$$|(a_{i+1} - w_{i+1}) - (a_i - w_i)| \geq o^*/N, \tag{28}$$

where o^*/N expresses the limiting angle of the structure. For our setting $o^* = 1$ corresponds to the common 45° bound for overhanging structures. While the upper bound

on the absolute value in the slope and curvature constraints can be reformulated as a two sided constraint

$$|g(s)| \leq g^* \ \rightarrow \ -g^* \leq g(s) \leq g^*,$$

this is not possible for a lower bound condition of type (28). Here the abs function needs to be approximated as

$$|g(s)| \approx \sqrt{g(s)^2 + \epsilon^2} - \epsilon,$$

which results in nonlinear local constraints.

For vertical structures we need to restrict for the left boundary only overhangs to the left

$$(a_{i+1} - w_{i+1}) - (a_i - w_i) \leq o^*/N \tag{29}$$

and overhangs to the right on the right boundary as

$$(a_{i+1} + w_{i+1}) - (a_i + w_i) \leq o^*/N. \tag{30}$$

Fig. 14 Overhang constraints for horizontal and vertical structures. Red lines show active overhang constraints, dashed orange lines show inactive overhang constraints, green dotted lines show interfaces where overhang constraints are not required. Note that the horizontal structure requires a support structure in the center
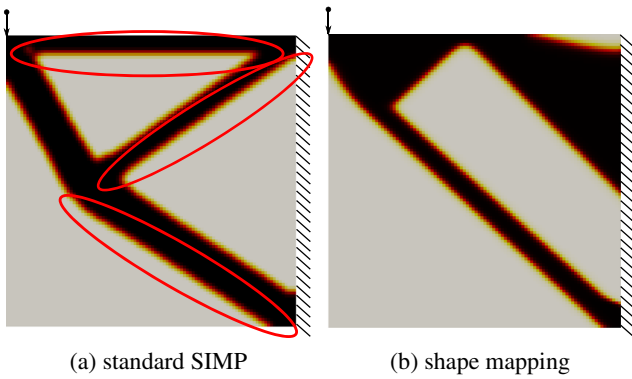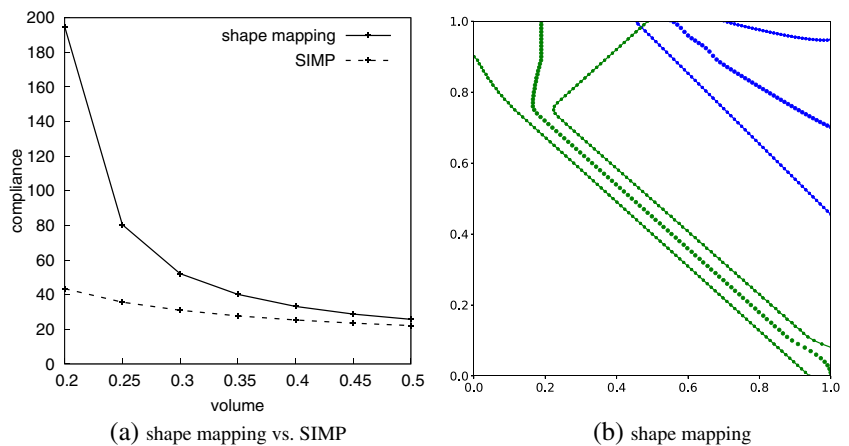
(a) standard SIMP   (b) shape mapping
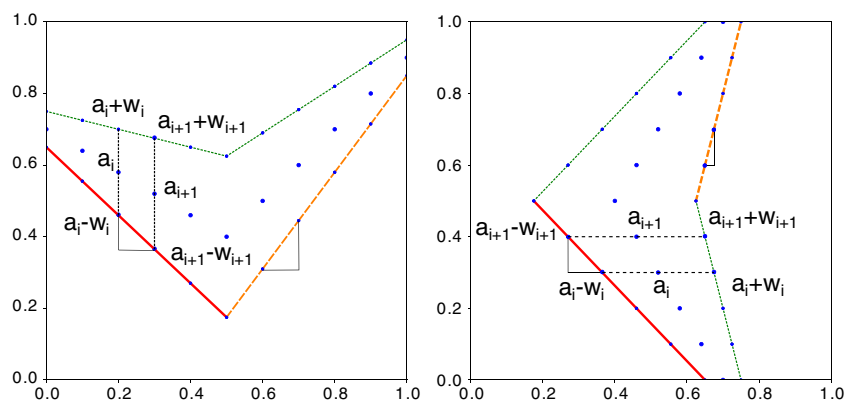
Fig. 15 **a** Classical topology optimization of a cantilever with vertical load on the upper left tip and full support on the right side with a volume constraint of 0.3. Areas with infeasible overhang are marked; **b** corresponding shape mapping with overhang constraints, see also Fig. 16b. $N = 100$, $\beta = 50$

This allows us to formulate the compliance minimization problem outlined in Fig. 15 with overhang constraints as

$$\min_{a,w} \quad f^\top u$$
$$\text{s.t.:} \quad K(\rho)\,u = f$$
$$\rho_e = T_e^\tau(a, w), \quad 1 \le e \le N^2$$
$$v(\rho) \le .3$$
$$|(a_{i+1} - w_{i+1}) - (a_i - w_i)| \ge 0.9/N, \quad i \in I_1$$
$$(a_{i+1} - w_{i+1}) - (a_i - w_i) \le 1.1/N, \quad i \in I_2$$
$$(a_{i+1} + w_{i+1}) - (a_i + w_i) \le 1.1/N, \quad i \in I_2$$
$$|a_{i-1} - 2\,a_i + a_{i+1}| \le .4/N, \quad i \in Y_1 \cup Y_2$$
$$|w_{i-1} - 2\,w_i + w_{i+1}| \le .5/N, \quad i \in Y_1 \cup Y_2$$
$$a_i \in [0, 1.5], \quad i \in K_1$$
$$a_i \in [0, 1], \quad i \in K_2$$
$$w_i \in [0.1, 1.1], \quad i \in K_1 \cup K_2,$$

with the additional index sets $K_1 = \{1, \ldots, N + 1\}$ and $K_2 = \{N + 2, \ldots, 2(N + 1)\}$ for the horizontal and the vertical structure, respectively. Note that we relax the 45° angle for the overhang constraints a little. Additional regularization is necessary in the form of rather relaxed curvature constraints for the nodal and profile variables. We allow the horizontal structure to move outside the design domain. The upper bound of the profile is practically unlimited, the volume constraint takes the limiting role.

The reference topology optimization without overhang constraints and the shape mapping solution with overhang constraints are shown in Fig. 15. The difference in obtainable compliance is shown in Fig. 16a, this depends strongly on the volume constraint. Note that we used a rather simple setup with only one horizontal and vertical structure.

As mentioned above, kinks for horizontal structures as shown in Fig. 14 are not directly prohibited. An indirect approach is to apply strong enough curvature constraints, enforcing an arc at the kink that would be infeasible with respect to the horizontal overhang constraints where the secants are too flat.

A direct variant to prevent kinks for horizontal structures is to replace (28) by linear monotonicity constraints. However, it is then necessary to decide from the outset whether a structure shall grow upwards

$$(a_{i+1} - w_{i+1}) - (a_i - w_i) \ge o^*/N$$

or vice versa

$$(a_i - w_i) - (a_{i+1} - w_{i+1}) \ge o^*/N.$$

Fig. 16 **a** Showing several topology optimization (w/o overhang constraints) and shape mapping problems (with overhang constraints) for different volume constraints; **b** The shape parameters corresponding to Fig. 15b

(a) shape mapping vs. SIMP   (b) shape mapping

Fig. 17 **a** Convergence history for the single and two structure cantilever from Figs. 4a and 10 and the SIMP reference Fig. 4c; **b** Convergence history for the square symmetry example in Fig. 13

(a) cantilever

(b) square symmetry
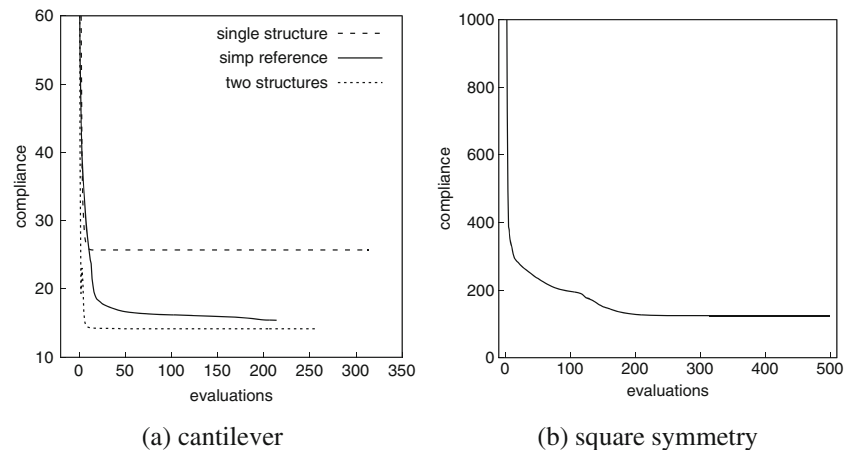
3.3 Convergence

In Fig. 17 we show convergence plots from selected examples. We use the SQP solver SNOPT[4] but the method of moving asymptotes could also be used. Additionally to SNOPT's KKT stopping criterion, we stop when there is successively no significant change in the cost function value.

Generally the design changes very fast toward the final design, the first iteration usually comes with the biggest change.

In contrast to standard density-based topology optimization, strong KKT optimality criteria are numerically difficult or impossible to reach. We repeated the single cantilever example from Fig. 4 with very strict stopping criteria with different choices of β for (6). Each design obtained in this way visually shows no difference to Fig. 4b. As in Fig. 5c we explore the gradient with respect to the profile variables for the converged design. While a constant gradient is to be expected, Fig. 18 shows the gradient to become more and more jagged with increasing β. We assume this behavior to be correlated with the problems to achieve a low numerical KKT optimality criterion, caused by a too steep hyperbolic tangent function in combination with a fixed discretization of the underlying mesh. Nevertheless, we do not observe a need for continuation of β. Of course this is only true if the required KKT condition is not to small.

4 Examples

In this section we present applications where we view shape mapping as a viable alternative approach to topology optimization.

[4]See Gill et al. (2002).

4.1 Phononic band gap optimization

Topology optimization of phononic band gap structures, introduced in Sigmund and Jensen (2003), yields periodic designs which suppress transmission of vibrations for a wide frequency range. However, the standard solutions are composed of solid material embedded within a weaker matrix material and are therefore bi-material designs.

It is inherently difficult to find connected solid/void band gap designs exhibiting a certain stiffness. Not only are the standard maximal band gap and maximal stiffness designs mutually exclusive, the band gap optimization is also known for non-smoothness issues caused by multiple and switching eigenvalues. Nevertheless, in Bilal and Hussein (2012) an in-plane design with a normalized band gap of 0.77 is presented as the best known connected design of its kind. Meta-heuristics have been applied to find the design.

With topology optimization, the requirement of a connected structure needs to be formulated directly or
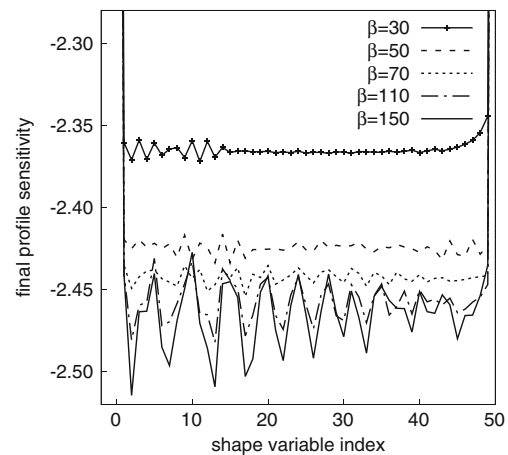
Fig. 18 Zoom on final profile sensitivity as in Fig. 5c with different β

Fig. 19 **a** The square
symmetric reference structure
obtained in Warmuth and
Körner (2015) in a tiled
visualization; **b** The dispersion
diagram shows that for all wave
directions the eigenfrequencies
up to the 8th mode are below
500 Hz and above 1000 Hz for
the 9th and higher modes

(a) repeated reference design


(b) dispersion diagram
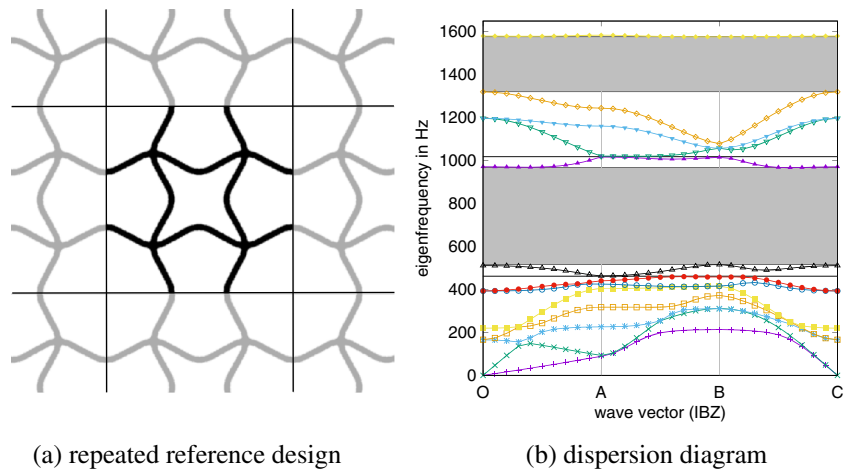
indirectly by the problem formulation. With parametric
shape optimization, the design space solely consists of
connected structures, so it is not necessary to model the
requirement.

Here we choose a sine like lattice structure from War-
muth and Körner (2015) as reference and initial design

which can be expressed, using square-symmetry, by a single
structure, see Fig. 19.

To explore the potential of the reference structure, we
restrict the design space to a vicinity of the reference nodal
shape parameters a_i^* extracted from Fig. 19a. The problem
formulation for the maximization of the relative band gap

Fig. 20 Optimized phononic
band gaps structure starting
from the design in Fig. 19. The
center nodes a_i are only allowed
to move within 20% of the
structural width

(a) density field

(b) shape variables

(c) repeated reference design

(d) dispersion diagram
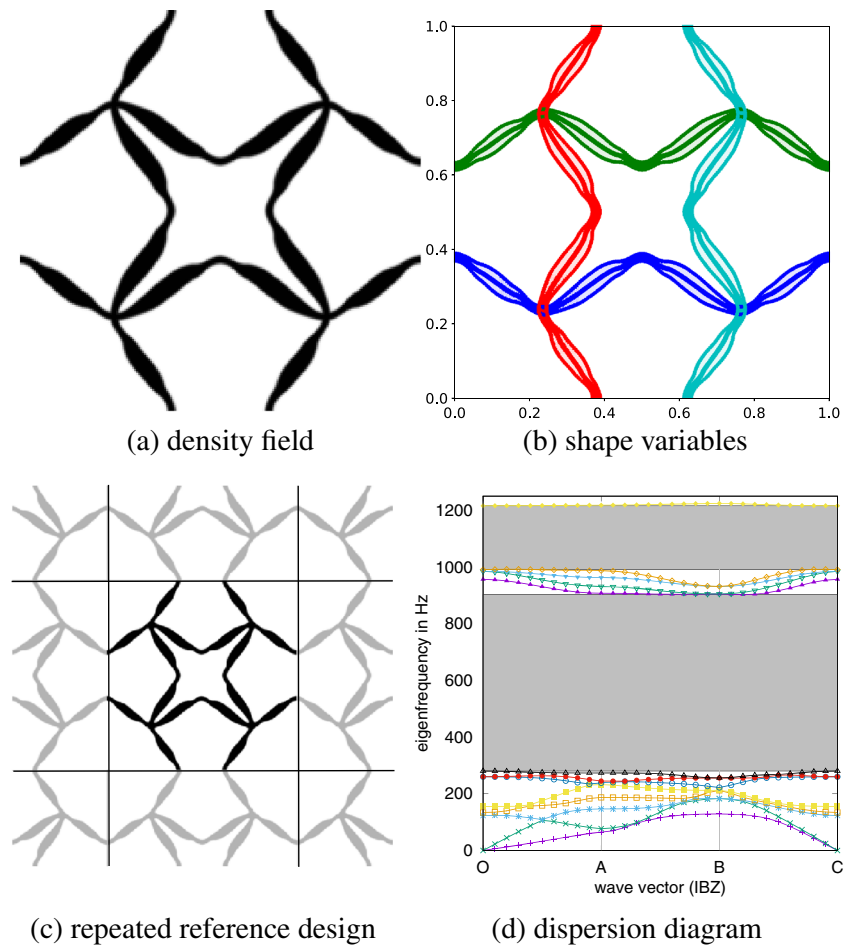
with two auxiliary variables γ (half band gap) and α (gap center frequency) between the 8th and 9th mode reads as:

$$\max_{a, w, \alpha, \gamma} \quad \frac{2\gamma}{\alpha - \gamma}$$

$$\text{s.t.:} \quad \omega_{jl} \leq \alpha - \gamma, \quad 1 \leq j \leq K, \quad 1 \leq l \leq 8$$

$$\omega_{jl} \geq \alpha + \gamma, \quad 1 \leq j \leq K, \quad 8 \leq l \leq 12$$

$$\left(K(K_j, \rho) - \omega_{jl}^2 M(\rho) \right) \Phi_{jl} = 0, \quad 1 \leq j \leq K, \quad 1 \leq l \leq 12$$

$$\rho_e = T_e^\tau(a, w)$$

$$|a_i - a_{i+1}| \leq 1.5/N$$

$$|w_i - w_{i+1}| \leq .5/N$$

$$|a_{i-1} - 2a_i + a_{i+1}| \leq .1/N$$

$$|w_{i-1} - 2w_i + w_{i+1}| \leq .1/N$$

$$|a_i - a_i^*| \leq 0.05$$

$$w_i \in [0.01, 0.05]^{N/2},$$

plus the square symmetry conditions from Section 3.2.2 for nodal and profile parameters. The resolution N is chosen to be 200 for a unit square, resulting in $N/2$ nodal and profile shape variables due to square symmetry, $\beta = 400$. K represents the number of discrete wave vectors to calculate. The result of the optimization is shown in Fig. 20.

The relative band gap is improved from 0.88 to 2.22, which corresponds to a normalized band gap $(2\gamma/\alpha)$ of 1.05. However without considering minimal feature size and stiffness, this cannot be directly compared with the result in Bilal and Hussein (2012).

Optimizing for lower modes even larger relative band gaps can be obtained. However, a full discussion of this issue would go beyond the scope of this presentation and will be studied in a forthcoming publication by the authors.

4.2 Boundary driven heat optimization

The following linear and static heat optimization example can be seen as a first step toward the optimization of a
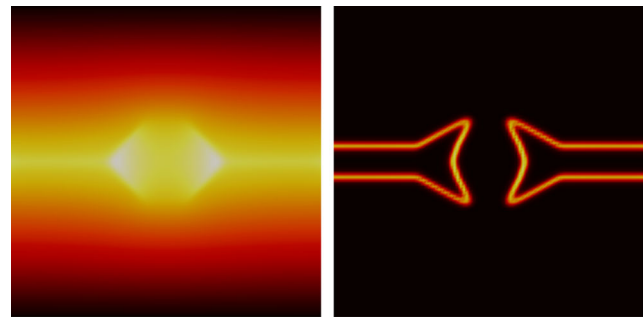

Fig. 22 Temperature for the design from Fig. 21. The right image shows the interface temperature subject to the tracking cost function. Perfect tracking cannot be achieved

catalyst optimization problem. We assume an exothermic reaction at the interface of a lattice representing the catalyst support structure. At the upper and lower boundary of a unit domain, homogeneous Dirichlet boundary conditions are applied.

For a boundary driven heat source we use nodal pseudo densities $d_j = D(\rho)$ for all nodes $1 \leq j \leq (N+1)^2$ calculated from the adjacent element pseudo densities. The heat source only heats the interface between solid and void. It can be formulated as the right hand side of the static heat state equation as

$$f_j = f^* 4 d_j (1 - d_j), \quad 1 \leq j \leq (N+1)^2,$$

with f^* a given constant heat source applied to a *grayness* term. The objective is to find a design which tracks the temperature at the interface to a given reference temperature u^*, e.g. because the temperature is ideal for the reaction to take place. It is expected that any interface too close to the homogeneous Dirichlet boundary conditions. will be cooled to a too low temperature and any interface too far from the boundary conditions is likely to be insufficiently cooled and therefore heated above u^*.

Fig. 21 Optimized density and structures for the interface driven heat tracking problem in Section 4.2. The profiles of one vertical and two horizontal structures are optimized. No symmetry conditions are applied. $N = 100$, $\beta = 100$
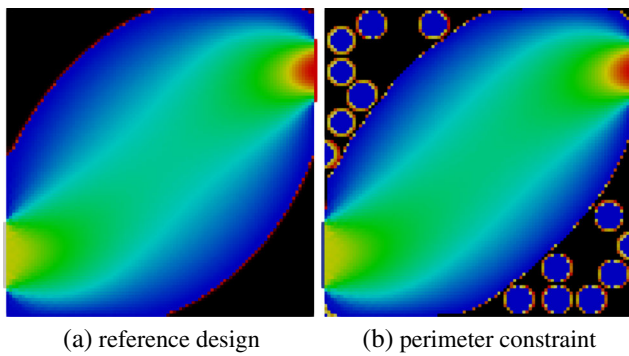
(a) reference design   (b) perimeter constraint
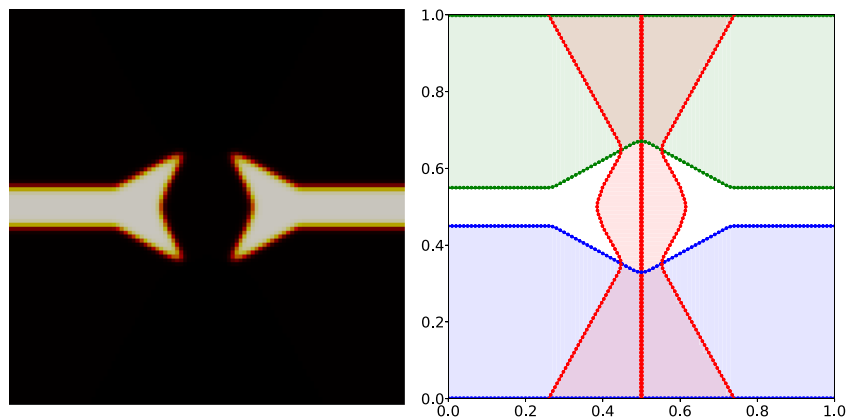
Fig. 23 **a** Solution of a standard minimal pressure topology optimization problem with active minimal volume bound $v(\rho) = 0.2$. The perimeter results in $q(\rho) = 0.011$; **b** Design for added perimeter constraint $q(\rho) = 0.033$ based on a Heaviside projection filter. The original pressure drop is 1% better than in (**b**)

The optimization problem reads as

$$\max_{\boldsymbol{w}} \quad \sum_j 4\, d_j (1 - d_j)(u_j - u^*)^2$$

$$\text{s.t.:} \quad \boldsymbol{K}(\rho)\,\boldsymbol{u} = \boldsymbol{f}$$

$$\rho_e = T_e^\tau(\boldsymbol{a}, \boldsymbol{w}), \quad 1 \le e \le N^2$$

$$d_j = D(\rho) \in [0,1]^{(N+1)^2}$$

$$|w_i - w_{i+1}| \le 1.1/N$$

$$|w_{i-1} - 2\,w_i + w_{i+1}| \le .5/N$$

$$w_i \in [0.05, 0.45]$$

$$a_i = 0, \quad i \in I_1$$

$$a_i = 1, \quad i \in I_2$$

$$a_i = .5, \quad i \in I_3,$$

with $I_1 = \{1, \dots, N+1\}$ and $I_2 = \{N+2, \dots, 2(N+1)\}$ the index sets of two horizontal structures (blue and green in Fig. 21b) and $I_3 = \{2(N+1)+1, \dots, 3(N+1)\}$ a vertical structure (red color).

The obtained result of the shape mapping problem is shown in Figs. 21 and 22. The benefit of shape mapping lies

here in the clear definition of the interface by the shape to density mapping T (6), where t_β strictly defines the width of the interface. It is noted that in such cases, where the objective is very sensitive with respect to intermediate pseudo density values classical density-based topology optimization tends to optimize merely the grayness of the interface rather than the topology. A rigorous treatment of stress constraints suffers from a similar issue, see e.g. Bruggi (2008).

4.3 LBM based flow optimization

Another route toward catalyst optimization is to maximize the length of the solid/void interface with a concurrent pressure drop minimization. We choose to model the fluid dynamics by the Lattice Boltzmann method based on the topology optimization approach given in Pingen et al. (2007). The state variables are the discrete $D2Q9$ probability distribution functions $\boldsymbol{f}$ from which the local pressure $p(\boldsymbol{f})$ can be calculated.

For the approximation of the perimeter we use the simple *taxicab* norm q, which counts the grayness difference over all element to element edges and is normalized to 1 for a perfect checkerboard structure. This structure is infeasible with shape mapping and regularized topology optimization.

$$q(\rho) = \frac{1}{2\,N(N-1)} \sum_{k=2}^N \sum_{l=1}^N |\rho_{kl} - \rho_{k-1,l}| + \sum_{k=1}^N \sum_{l=2}^N |\rho_{kl} - \rho_{k,l-1}|.$$

The taxicab norm favors 45° angles; a discussion of this issue and higher order perimeter approximations is given in Petersson et al. (1999).

We optimize the profiles of two horizontal and two vertical structures. To prevent covering the inflow and outflow with the vertical structures, in each area, we set the structure center nodes a far outside of the design domain.

Fig. 24 Pressure drop minimization with given active minimal perimeter bound $q(\rho) \ge 3.3/N$. The inflow is on the lower left side, outflow on the upper right side. The velocity magnitude of the laminar flow is depicted on the left. On the right the optimized profiles of two horizontal (blue and green) and two vertical structures (red and cyan) are shown. The center nodes of the structures were not subject to optimization
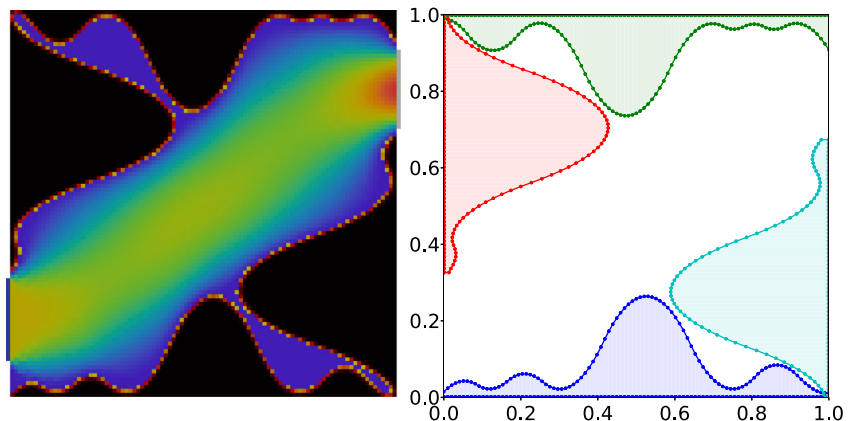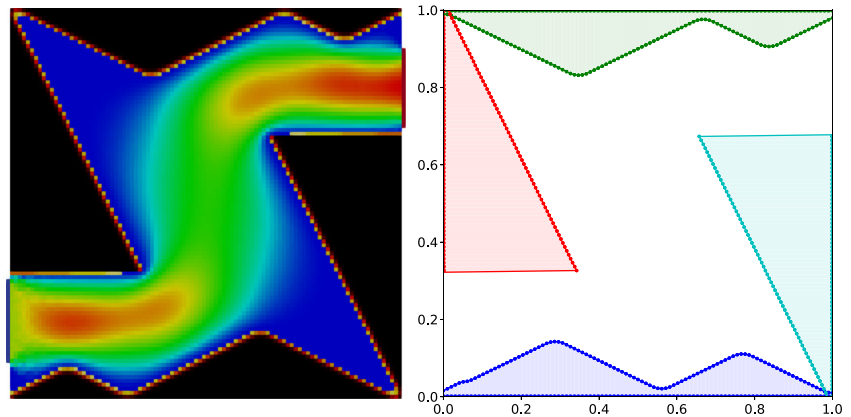
Fig. 25 Modified LBM pressure drop minimization with active perimeter bound $q(\boldsymbol{\rho}) \geq 2.8/N$ and additional slope constraints (34). While the shape mapping result in Fig. 24 comes with a pressure drop 30% larger than the reference design in Fig. 23a, the pressure drop obtained here is 166% larger

The optimization problem reads as

$$\min_{\boldsymbol{w}} \quad \frac{1}{N_{\text{inlet}}} \sum_{j}^{\text{inlet}} p_j(\boldsymbol{f}) - \frac{1}{N_{\text{outlet}}} \sum_{j}^{\text{outlet}} p_j(\boldsymbol{f})$$

$$\text{s.t.:} \quad \boldsymbol{R}(\boldsymbol{f}(\boldsymbol{\rho}))) = \boldsymbol{0}$$
$$\rho_e = T_e^\tau(\boldsymbol{a}, \boldsymbol{w})$$
$$q(\boldsymbol{\rho}) \geq 3.3/N$$
$$|w_{i-1} - 2\,w_i + w_{i+1}| \leq .4/N$$
$$w_i \in [0, 0.7].$$

The problem is discretized with $N = 100$, $\beta = 150$. The multi-objective problem is solved by minimizing the pressure drop for a given lower perimeter bound. We note that a single straight interface $\sum_{l=1}^{N} |\rho_{k\,l} - \rho_{k-1\,l}|$ has a perimeter value $q(\boldsymbol{\rho}) = .5/N$.

A standard pressure drop minimization by topology optimization without explicit perimeter control results in a perimeter of $\approx 1.1/N$ for $v(\boldsymbol{\rho}) = 0.2$, see Fig. 23a. Compared to the reference solution in Fig. 23a, the pressure drop for the design in Fig. 24 is 30% larger for a three times larger perimeter $q(\boldsymbol{\rho}) = 3.3/N$.

In Fig. 23b we show the result of a topology optimization problem with the same perimeter bound as for the shape mapping problem in Fig. 24. To this end, we applied a Heaviside projection filter (Guest et al. 2004). The minimal pressure is only slightly changed with respect to the reference design but holes are formed which are not connected to the in- or outflow and thus not accessible for the fluid.

However, we should note that in the shape mapping formulation cavities with almost no flow are also formed, see Fig. 24. This reveals a limitation of the presented method; feature size of the structures can be formulated but there is no formulation for the gap between structures. Between two structures of common orientation this could easily be formulated as

$$(a_{B+i} - w_{B+i}) - (a_{A+i} + w_{A+i}) \geq g^*, \quad 1 \leq i \leq N+1, \tag{31}$$

where the variables for the lower/left structure start with index $A - 1$ and the for the upper/right structure with $B - 1$, respectively. In the present example with vertical and horizontal structures one could declare void regions as

$$a_i + w_i \leq b_i^*, \quad i \in V_1 \tag{32}$$
$$a_i - w_i \geq b_i^*, \quad i \in V_2, \tag{33}$$

where V_1 and V_2 are index sets such that b_i^* describes a void geometry. An obvious drawback of that approach for the LBM problem is clearly, that such a fixed void area is difficult to define a priori. Alternatively slope constraints can be applied, however, again the choice of the slope bound is not easy to determine a priori. A bound for $45°$ still allows partially common interface for the structures, but numerical experiments show for the addition of constraints

$$|a_{i+1} - a_i| \leq 1/N \tag{34}$$

in Fig. 25 that no thin cavities occur, however we can only achieve a maximal perimeter of $\approx 2.8/N$ which comes with a poor pressure drop 166% larger than the reference design. Obviously, the pressure drop minimization problem with prescribed perimeter is a challenging problem. While a naive density-based topology optimization expectedly fails, also a shape mapping formulation yielding satisfactory results could not be found.

5 Conclusion and outlook

We have presented a parametric shape optimization where horizontal and vertical structures are mapped to a pseudo density field on a fixed regular mesh. The structures are characterized by central nodal and profile thickness variables associated which the grid nodes of the underlying mesh.

The proposed method belongs to a class of geometry projection to fictitious domain methods. Hence it shares the property that the differentiable structure to mesh mapping results in a pseudo density field. Such a pseudo density field

is also used in classical SIMP based topology optimization. Therefore an existing density-based topology optimization implementation can be reused, including sensitivity analysis and calculation of gradients for arbitrary problems.

The approach is related both to classical parametric shape optimization and to rising field of geometry projection methods. Comparing this approach with classical parametric shape optimization, no remeshing is required. However, the sharp boundaries are lost as the structure to shape mapping introduces blurred interfaces. The volume can easily be calculated based on the pseudo density field. If we compare the structure to pseudo density mapping with geometry projection, as in Norato et al. (2015) or Hoang and Jang (2016), it is performed in a similar manner, but our design representation does not allow arbitrary placement and rotation of (many) sizable geometric objects in the design domain.

Existing geometry projection methods either define the design or void area by the union of explicitly given simple geometries, what we consider as topology optimization, or perform shape optimization with an implicitly given shape representation. In both cases, essentially arbitrary designs are possible. Whereas the parametrization by horizontal and vertical structures results in a significantly limited design space. However, we see the limited design space in combination with design regularization[5] as beneficial for specific problem classes. In these cases a free topology optimization tends to result in undesired designs and modeling the actual requirements is non-trivial. In contrary, it is unlikely that the presented method shows significant benefit for problems which can already be solved painless with established methods. Three examples showing potential for our method are given in Section 4.

For the phononic band gap maximization, we require horizontally and vertically connected structures, while isolated unconnected solid material would exhibit dramatically superior performance. By structural parametrization the connection is compulsory with indirect feature size control via bounds on the profile variables.

For the boundary driven heat source optimization problem, we benefit from an explicit interface modeling, leaving no room for the optimizer to satisfy the temperature tracking by tuning intermediate material only. We note that precise interface control is also possible in topology optimization by Heaviside projection filtering and robust formulations as in Wang et al. (2011) with a careful continuation strategy for the projection parameter.

For the indirect perimeter maximization flow problem, topology optimization would result in undesired cavities.

This can be avoided by structural parametrization. However, care is still required, as almost isolated cavities are formed, see Fig. 24.

The simple parametrization of horizontal and vertical structures by center node and profile variables shows itself to be surprisingly versatile. Fixing either the central nodal variables or the profile variables or bounding them in the vicinity of some reference design allows easy modeling of requirements beyond classical modeling of topology optimization problems. Despite the limited design space, surprisingly complex designs are found, including different topologies. Only orthogonal parametrization within a rectangular design domain has been considered. A more a more complex analytical domain could be embedded within a larger shape domain, see the overhang and LBM example. A more complex shape parametrization, e.g. diagonal or curved, could be realized by an additional coordinate transformation. However, we did not investigate this at present time.

References

Allaire G, Jouve F, Michailidis G (2016) Thickness control in structural optimization via a level set method. Struct Multidiscip Optim 53(6):1349–1382

Andreassen E, Clausen A, Schevenels M, Lazarov B, Sigmund O (2011) Efficient topology optimization in matlab using 88 lines of code. Struct Multidiscip Optim 43(1):1–16

Bendsøe MP (1989) Optimal shape design as a material distribution problem. Struct Multidiscip Optim 1:193–202

Bilal OR, Hussein MI (2012) Topologically evolved phononic material: breaking the world record in band gap size. In: SPIE OPTO, International society for optics and photonics, pp 826,911–826,911

Braibant V, Fleury C (1984) Shape optimal design using b-splines. Comput Methods Appl Mech Eng 44(3):247–267

Bruggi M (2008) On an alternative approach to stress constraints relaxation in topology optimization. Struct Multidiscip Optim 36(2):125–141

Bruns TE, Tortorelli DA (2001) Topology optimization of non-linear elastic structures and compliant mechanisms. Comput Methods Appl Mech Eng 190(26-27):3443–3459

Christiansen AN, Bærentzen JA, Nobel-Jørgensen M, Aage N, Sigmund O (2015) Combined shape and topology optimization of 3d structures. Comput Graph 46:25–35

Dunning PD (2017) Design parameterization for topology optimization by intersection of an implicit function. Comput Methods Appl Mech Eng 317:993–1011

Gangl P, Langer U, Laurain A, Meftahi H, Sturm K (2015) Shape optimization of an electric motor subject to nonlinear magnetostatics. SIAM J Sci Comput 37(6):B1002–B1025

---

[5]Slope constraints, curvature constraints and possibly overhang constraints.

Gaynor AT, Guest JK (2016) Topology optimization considering overhang constraints: Eliminating sacrificial support material in additive manufacturing through design. Struct Multidiscip Optim 5(54):1157–1172

Gersborg AR, Andreasen CS (2011) An explicit parameterization for casting constraints in gradient driven topology optimization. Struct Multidiscip Optim 44(6):875–881

Gill PE, Murray W, Saunders MA (2002) SNOPT: An SQP algorithm for large-scale constrained optimization. SIAM J Optim 12(4):979–1006

Guest JK (2009) Imposing maximum length scale in topology optimization. Struct Multidiscip Optim 37(5):463–473

Guest J, Prévost J, Belytschko T (2004) Achieving minimum length scale in topology optimization using nodal design variables and projection functions. Int J Numer Methods Eng 61(2):238–254

Haftka RT, Grandhi RV (1986) Structural shape optimization: a survey. Comput Methods Appl. Mech Eng 57(1):91–106

Haslinger J, Mäkinen R (2003) Introduction to Shape Optimization: Theory, vol 7. Siam

Hoang VN, Jang GW (2016) Topology optimization using moving morphable bars for versatile thickness control. Computer Methods in Applied Mechanics and Engineering

Imam MH (1982) Three-dimensional shape optimization. Int J Numer Methods Eng 18(5):661–673

Langelaar M (2017) An additive manufacturing filter for topology optimization of print-ready designs. Struct Multidisc Optim 55(3):871–883

Lazarov B, Wang F, Sigmund O (2016) Length scale and manufacturability in density-based topology optimization. Arch Appl Mech 86(1-2):189–218

Le C, Bruns T, Tortorelli D (2011) A gradient-based, parameter-free approach to shape optimization. Comput Meth Appl Mech Eng 200(9):985–996

Maute K, Ramm E (1995) Adaptive topology optimization. Struct Optim 10(2):100–112

Norato J, Haber R, Tortorelli D, Bendsøe MP (2004) A geometry projection method for shape optimization. Int J Numer Methods Eng 60(14):2289–2312

Norato J, Bell B, Tortorelli D (2015) A geometry projection method for continuum-based topology optimization with discrete elements. Comput Methods Appl Mech Eng 293:306–327

Novotny AA, Sokołowski J (2012) Topological derivatives in shape optimization. Springer Science & Business Media, Berlin

Petersson J, Sigmund O (1998) Slope constrained topology optimization. Int J Numer Methods Eng 41:1417–1434

Petersson J, Beckers M, Duysinx P (1999) Almost isotropic perimeters in topology optimization: Theoretical and numerical aspects. In: Third world congress of structural and multidisciplinary optimization

Pingen G, Evgrafov A, Maute K (2007) Topology optimization of flow domains using the lattice Boltzmann method. Struct Multidiscip Optim 34(6):507–524

Saxena A (2008) A material-mask overlay strategy for continuum topology optimization of compliant mechanisms using honeycomb discretization. J Mech Des 130(8):082,304

Saxena A (2011) Topology design with negative masks using gradient search. Struct Multidiscip Optim 44(5):629–649

Semmler J, Pflug L, Stingl M, Leugering G (2015) Shape optimization in electromagnetic applications. In: New trends in shape optimization. Springer, pp 251–269

Sigmund O (2001) A 99 Line topology optimization code written in MATLAB. Struct Multidiscip Optim 21:120–127

Sigmund O (2007) Morphology-based black and white filters for topology optimization. Struct Multidiscip Optim 33(4):401–424

Sigmund O, Jensen JS (2003) Systematic design of phononic band-gap materials and structures by topology optimization. Philos Trans R Soc Math Phys Eng Sci 361(1806):1001–1019

Sigmund O, Maute K (2013) Topology optimization approaches. Struct Multidiscip Optim 48(6):1031–1055

Sigmund O, Petersson J (1998) Numerical instabilities in topology optimization: A survey on procedures dealing with checkerboards, mesh-dependencies and local minima. Struct Multidiscip Optim 16:68–75

Sokolowski J, Zolesio JP (1992) Introduction to shape optimization. In: Introduction to shape optimization. Springer, pp 5–12

Svanberg K (1987) The method of moving asymptotes-a new method for structural optimization. Int J Numer Methods Eng 24(2):359–373

van Dijk NP, Maute K, Langelaar M, Van Keulen F (2013) Level-set methods for structural topology optimization: a review. Struct Multidiscip Optim 48(3):437–472

Wang F, Lazarov B, Sigmund O (2011) On projection methods, convergence and robust formulations in topology optimization. Struct Multidiscip Optim 43(6):767–784

Warmuth F, Körner C (2015) Phononic band gaps in 2d quadratic and 3d cubic cellular structures. Materials 8(12):8327–8337

Yurkin MA, Hoekstra AG (2007) The discrete dipole approximation: an overview and recent developments. J Quant Spectrosc Radiat Transfer 106(1):558–589

Zhang W, Zhang J, Guo X (2016) Lagrangian description based topology optimization: A revival of shape optimization. J Appl Mech 83(4):041,010

Zhou M, Lazarov B, Wang F, Sigmund O (2015) Minimum length scale in topology optimization by geometric constraints. Comput Methods Appl Mech Eng 293:266–282